



## Analytical simulation of groundwater flow and land surface effects on thermal plumes of borehole heat exchangers



Jaime A. Rivera <sup>a,\*</sup>, Philipp Blum <sup>b</sup>, Peter Bayer <sup>a</sup>

<sup>a</sup> ETH Zürich, Department of Earth Sciences, Sonneggstrasse 5, 8092 Zurich, Switzerland

<sup>b</sup> Karlsruhe Institute of Technology (KIT), Institute for Applied Geosciences (AGW), Kaiserstraße 12, 76131 Karlsruhe, Germany

### HIGHLIGHTS

- A new analytical solution for simulating shallow geothermal systems is presented.
- The solution accounts for long-term changes in land use and groundwater flow.
- The approach is verified with a numerical model and validated in a case study.
- Land use changes and horizontal advection can overprint anomalies induced by BHEs.

### ARTICLE INFO

#### Article history:

Received 12 September 2014

Received in revised form 4 February 2015

Accepted 8 February 2015

#### Keywords:

Geothermal energy

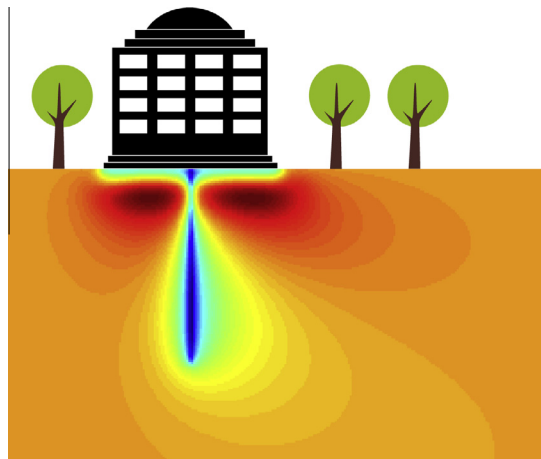
Ground source heat pump system

Heat transport

Land use

Advection

### ABSTRACT



A new analytical model is presented for simulation of ground thermal effects from vertical borehole heat exchangers (BHEs). It represents an extension of the moving line source equation and efficiently describes the coupled transient effects from geothermal energy extraction, subsurface heat conduction, horizontal groundwater flow and spatially variable land use. It is successfully verified by comparison with an equivalent numerical model and validated by application to a field case with detailed long-term temperature monitoring. Non-dimensional sensitivity analysis reveals the coupled influence of advection and conduction for different assumptions of the land surface. Especially accelerated heat flux from asphalt or buildings at the land surface is shown to have a remarkable impact on the thermal conditions in the ground. Together with the flow velocity of the groundwater, it determines the intensity, form and steady-state of the thermal anomaly induced from BHE operation.

© 2015 Elsevier Ltd. All rights reserved.

\* Corresponding author. Tel.: +41 44 6332594; fax: +41 44 6331108.

E-mail address: [jaime.rivera@erdw.ethz.ch](mailto:jaime.rivera@erdw.ethz.ch) (J.A. Rivera).

## Nomenclature

|               |  |                      |  |
|---------------|--|----------------------|--|
| $a$           | thermal diffusivity ( $\text{m}^{-2} \text{s}$ )                                     | $x, y, z$            | single space coordinates where temperature is evaluated (m)                      |
| $b_1, b_2$    | scaling parameters for top boundary temperature functions                            | $x', y', z'$         | single space coordinates where heat sources are located (m)                      |
| $c_w, c_s$    | volumetric heat capacity of water and of solids ( $\text{MJ m}^{-3} \text{K}^{-1}$ ) | $\mathbf{X}$         | dimensionless form of $\mathbf{x}$   |
| $C_p$         | specific heat capacity of the porous medium ( $\text{J kg}^{-1} \text{K}^{-1}$ )     | $\mathbf{X}'$        | dimensionless form of $\mathbf{x}'$  |
| $F_o$         | Fourier number   | $X, Y, Z$            | dimensionless form of $x, y, z$  |
| $F_o^w$       | frequency-modified $F_o$   | $X', Y', Z'$         | dimensionless form of $x', y', z'$   |
| $f$           | spatial distribution function of instantaneous sources or sinks                      | $z^*$                | characteristic length (m)  |
| $G$           | Green's function   | <i>Greek symbols</i> |  |
| $g$           | spatial distribution function of continuous sources or sinks                         | $\theta$             | dimensionless temperature  |
| $H$           | borehole length (m)  | $\lambda$            | thermal conductivity of porous medium ( $\text{W m}^{-1} \text{K}^{-1}$ )        |
| $J$           | dimensionless form of $j$  | $\vartheta$          | analytical temperature solution ( $^{\circ}\text{C}$ )                           |
| $j$           | main integrand function within the MFLS solution                                     | $\rho$               | density ( $\text{kg m}^{-3}$ )   |
| $k$           | geothermal gradient ( $^{\circ}\text{C m}^{-1}$ )                                    | $\tau$               | time at which a heat pulse is released (s)                                       |
| $L$           | phase shift of top boundary temperature functions                                    | $\varphi$            | top boundary temperature function ( $^{\circ}\text{C}$ )                         |
| $n$           | normal vector to the plane where heat sources are located                            | $\emptyset$          | dimensionless top boundary temperature function                                  |
| $n_e$         | effective porous medium porosity   | $\Delta\theta$       | dimensionless temperature change   |
| $OH$          | operational hours of a heat pump (h)   | $\omega$             | frequency ( $\text{month}^{-1}$ or $\text{year}^{-1}$ )                          |
| $Pe$          | Péclet number  | <i>Subscripts</i>    |  |
| $q_d$         | Darcy velocity ( $\text{m s}^{-1}$ )   | $a, b$               | lower ( $a$ ) and upper ( $b$ ) coordinates of an area with distinctive land use |
| $q_L$         | heat flow rate per unit length ( $\text{W m}^{-1}$ )                                 | $c$                  | continuous heat source   |
| $R$           | dimensionless form of $r$  | $lu$                 | land use   |
| $r$           | radial distance from the borehole (m)  | $o$                  | initial conditions   |
| $T$           | temperature in the porous medium ( $^{\circ}\text{C}$ )                              | $p$                  | bulk porous medium property  |
| $T_s$         | ground surface temperature ( $^{\circ}\text{C}$ )                                    | $tb$                 | top boundary heat source   |
| $T_m$         | arbitrary reference temperature ( $^{\circ}\text{C}$ )                               | <i>Abbreviations</i> |  |
| $T_{Pe}$      | temperature calculated for a given $Pe$ ( $^{\circ}\text{C}$ )                       | BHE                  | borehole heat exchanger  |
| $t$           | time (s)   | FLS                  | finite line source   |
| $t_o$         | period of top boundary temperature functions (months or years)                       | GWF                  | groundwater flow   |
| $u$           | integration variable   | GSHP                 | ground source heat pump  |
| $v_t$         | effective thermal velocity ( $\text{m s}^{-1}$ )                                     | GST                  | ground surface temperature   |
| $\mathbf{x}$  | coordinates vector where temperature is evaluated (m)                                | MFLS                 | moving finite line source  |
| $\mathbf{x}'$ | coordinates vector where a heat source is located (m)                                | TDP                  | temperature depth profile  |

## 1. Introduction

Borehole heat exchangers (BHE) represent by far the most frequent geothermal applications [1]. In vertical boreholes, plastic tubes are installed, where a heat carrier fluid is circulated. This yields a well-controlled closed system, which exchanges heat with the ground without transfer of mass. The heat carrier fluid commonly feeds an aboveground heat pump that supplies low-temperature heating systems to buildings. Borehole length and number are tailored to a given heating and cooling demand. The boreholes are drilled to depths of tens to hundreds of meters and typically operated for decades [2–5].

BHEs are often applied for heating only, and annual heat exchange with the ground is, therefore, not balanced. Since the usually dominant transport mechanism in the ground, heat conduction, is a slow process, energy deficits are generated, and thermal anomalies develop around the boreholes. Rybach and Eugster [6] estimate the duration of thermal recovery as least as long as the time of operation. This has to be accounted for in design of individual BHE applications, and is a crucial aspect when multiple neighboring installations are operated [7]. Especially in many cities of central and northern Europe, the growing density of BHEs is critically watched [8]. Regulations are sparsely enforced to

constrain proliferation, such as minimum distances between adjacent systems and ground temperature thresholds. Recent surveys show that such directives are convenient, however, are also detached from the relevant thermal processes and factors [9,10]. Long-term thermal effects in the vicinity of BHEs are rarely continuously monitored such as at the Elgg site, Switzerland [6], and the field site Bad Wurzach, Germany [11]. Despite decades of experience, there exists no study that provides insight in the temperatures that really evolve from long-term operation of densely arranged BHE applications. Hence, analytical and numerical heat transport models are currently the most important means for predicting future conditions in the ground [12].

There exists a broad range of different modeling techniques and the most common approaches are based on Kelvin's line source theory [13–16]. In such (semi-) analytical line source models, the ground temperature field around the borehole is a function of radius and time, calculated based on the heat extraction (or injection) rate. In order to account for the axial effects at the borehole toe, the finite line source model is used and this variant is customarily employed for BHE planning [17,18]. Relying on a model that only addresses conductive heat transport, however, is not always advisable. Horizontal groundwater can additionally carry heat to the boreholes, and this advective transport component is

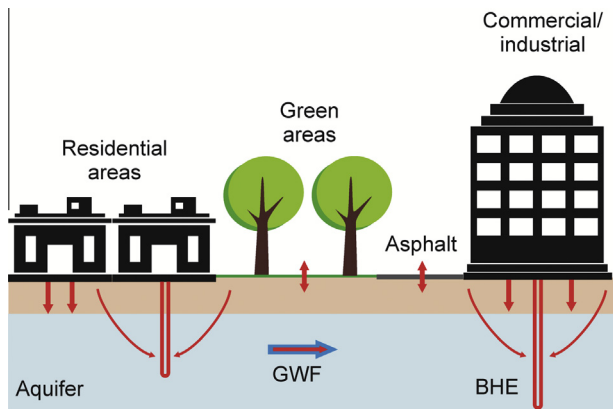


**Fig. 1.** Schematic cross section showing land cover variability and geothermal use in urban areas (red arrows indicate heat flow; GWF: ground water flow direction). (For interpretation of the references to colour in this figure legend, the reader is referred to the web version of this article.)

implemented in the moving line source model [19–21]. The role of advection was studied in several shallow geothermal applications. It has been shown that through groundwater flow heat extraction is more effective, and thermal anomalies are less pronounced, but potentially deviated in downstream direction [22–28]. This is crucial when regulative frameworks are defined, and the BHE density and arrangement has to be adjusted to the ambient groundwater flow regime instead of applying a static radial distance restriction [29]. Aside from this, description of thermal transport in the ground by conduction only results typically in a conservative evaluation of thermal BHE effects [30,31]. This ultimately means an underestimation of the geothermal potential and an oversizing of ground source heat pump (GSHP) systems [2].

Another aspect that possibly enhances the geothermal potential in cities is the accumulation of anthropogenic and waste heat in urban ground [32–36]. In built-up areas, heat migrates from the basement of buildings in the ground, and pavements accelerate ground heat gain from solar radiation [37–40] (see Fig. 1). Additional heat sources are infrastructural ground installations, such as subway tunnels, buried district heating, sewage networks, and also geothermal installations, such as aquifer thermal energy storage (ATES), groundwater heat pump and GSHP systems [38]. Bandos et al. and Santander et al. [41,42] introduced a finite line source that can handle conductive heat flow, a vertical geothermal gradient and, as top boundary, the vertical influence from the ground surface. Bandos et al. [42] demonstrated that by considering a time-dependent top boundary condition in the line source model, the effects from ambient temperature variations can be included in thermal response test (TRT) interpretation. In a related study on the design of foundation power transmission towers, Duan and Naterer [43] superimposed the transient finite line source and an equation describing a seasonal top boundary condition to reproduce experimental data. None of these analytical approaches, however, can be used to also simulate the effect of groundwater flow.

In the present study, a new analytical framework is presented that is based on the moving line source and able to quantify the effects of different land use types. In many cities that face a growing number of geothermal applications, such as Switzerland, the Netherlands [44] and others of the European Union [45], surface-near productive aquifers exist. Our objective is using this equation to reveal the combined effect of ground heat conduction and advection, when BHEs are operated in built-up areas with pronounced vertical conductive heat flux. By spatial and temporal superpositioning, time-dependent processes and spatially variable

land use types, which are characteristic in urban environments, can be simulated in a flexible way. This expands the application window of analytical equations as fast but simplifying alternatives to generally applicable numerical models [46].

First the new analytical model is introduced and then verified using a numerical heat transport model. Subsequently, the influence of changing land use types and groundwater flow velocities is comprehensively studied using a dimensional analysis. Finally, the analytical model is also validated and further investigated using the Elgg field test site in Switzerland under conductive and advective heat flow conditions. At this test site, ground temperature profiles at close distances from a BHE are repeatedly measured over a time span of 15 years [6].

## 2. Methodology

We propose a new analytical solution that complements the moving line source model by incorporating spatial and temporal variability of ground surface temperature (GST). The solution is suitable for modeling the effect of spatial land use variability, which is typical in urban environments, on borehole heat exchangers (BHEs). The conduction-advection problem is formulated in a semi-infinite space, in which specific Green's functions represent complex top boundary temperature conditions, continuous sources and sinks within the domain, as well as the initial temperature state.

For the analytical simulation, we assume that the ground can be approximated as semi-infinite, homogeneous and fully saturated porous medium. This corresponds to similar assumptions in related studies [13,14,18,47,48]. The top boundary (i.e., ground surface) is defined as 1st type or prescribed temperature condition. Within this framework, the BHE is modeled as a finite line source with constant heat flow rate. Furthermore, a steady state and uniform horizontal groundwater flow regime is applied. Some line source models also include mechanical dispersion (e.g. [49]), however, the present work focuses on advective heat flux from groundwater flow, and therefore dispersion effects are not considered (see also [27]). As is common in these models, thermal properties are set independent of temperature changes. Hecht-Méndez et al. [50], for instance, emphasize that the inaccuracies of BHE simulation, from assuming a constant groundwater viscosity and when ignoring buoyancy effects, are only minor within the temperature range shallow BHEs are operated.

Under these conditions, the temperature response within the half-space can be written as the superposition of any given initial thermal conditions ( $\vartheta_o$ ), known continuous sources or sinks ( $\vartheta_c$ ) and top boundary effects ( $\vartheta_{tb}$ ):

$$T(\mathbf{x}, \mathbf{x}', t) = \vartheta_o(\mathbf{x}, \mathbf{x}', t) + \vartheta_c(\mathbf{x}, \mathbf{x}', t) + \vartheta_{tb}(\mathbf{x}, \mathbf{x}', t) \quad (1)$$

where ( $\vartheta_o + \vartheta_c$ ) and  $\vartheta_{tb}$  are the solutions for the homogeneous and nonhomogeneous boundary-value problems of heat conduction respectively [13,51]. In Eq. (1), the individual responses are given in terms of the Green's function for the specific problem. For a half-space, this Green's function for an unitary and instantaneous heat pulse located at the point  $\mathbf{x}'$  at time  $\tau$  reads [13]:

$$G(\mathbf{x}, \mathbf{x}', t - \tau) = \frac{1}{8\rho C_p [\pi a(t - \tau)]^{3/2}} \times \left\{ \exp \left[ -\frac{(x - x')^2 + (y - y')^2 + (z - z')^2}{4a(t - \tau)} \right] - \exp \left[ -\frac{(x - x')^2 + (y - y')^2 + (z + z')^2}{4a(t - \tau)} \right] \right\} \quad (2)$$

The temperature response in the ground, due to a top boundary temperature  $\varphi(x', y', \tau)$ , is obtained through the superposition of continuous instantaneous doublets with intensity  $a\varphi(x', y', \tau)$  distributed over the boundary plane (here the plane  $z = 0$ ) as follows [13]:

$$\begin{aligned} \vartheta_{tb}(\mathbf{x}, \mathbf{x}', t) &= a \int_0^t \int_{x'} \int_{y'} \varphi(x', y', \tau) \left( \frac{\partial G}{\partial n} \right) dy' dx' d\tau \\ &= \frac{z}{8(\pi a)^{3/2}} \int_0^t \int_{x'} \int_{y'} \frac{\varphi(x', y', \tau)}{(t-\tau)^{5/2}} \\ &\quad \times \exp \left[ -\frac{(x-x')^2 + (y-y')^2 + z^2}{4a(t-\tau)} \right] dx' dy' d\tau, \quad z > 0 \end{aligned} \quad (3)$$

The temperature response due to unitary and continuous thermal sources or sinks, whose spatial distribution is given by  $g(\mathbf{x}')$ , is obtained through the superposition of continuous heat sources as follows:

$$\vartheta_c(\mathbf{x}, \mathbf{x}', t) = \int_0^t \left( \int_{x'} G(\mathbf{x}, \mathbf{x}', t-\tau) g(\mathbf{x}') dx' \right) d\tau \quad (4)$$

Finally, if the initial conditions are given by a temperature distribution  $f(\mathbf{x}')$ , the associated temperature response is

$$\vartheta_o(\mathbf{x}, \mathbf{x}', t) = \int_{x'} G(\mathbf{x}, \mathbf{x}', t) f(\mathbf{x}') dx' \quad (5)$$

There exist special solutions to this problem. When the initial conditions are determined by the geothermal gradient  $k$  and a known surface temperature  $T_s$ , the solution  $\vartheta_o$  becomes [13]

$$\vartheta_o(z, t) = T_s \operatorname{erf} \left( \frac{z}{\sqrt{4at}} \right) + kz \quad (6)$$

whose dimensionless form can be expressed as

$$\theta_o(F_o) = \frac{\vartheta_o - kz}{T_s} = \operatorname{erf} \left( \sqrt{\frac{1}{4F_o}} \right) \quad (7)$$

where  $F_o = \frac{az}{\alpha t}$  is the Fourier number. For continuous sources distributed along a finite line, the solution  $\vartheta_c$  becomes the finite line source (FLS) model [17] or its moving version (MFLS) [21] when groundwater flow is accounted for:

$$\vartheta_c(\mathbf{x}, \mathbf{x}', t) = \frac{q_L}{2\pi\lambda_p} \exp \left( \frac{v_t x}{2a} \right) \left[ \int_0^H j(\mathbf{x}, \mathbf{x}', t) dz' - \int_{-H}^0 j(\mathbf{x}, \mathbf{x}', t) dz' \right] \quad (8)$$

$$j(\mathbf{x}, \mathbf{x}', t) = \frac{1}{4r} \left[ \exp \left( -\frac{v_t r}{2a} \right) \operatorname{erfc} \left( \frac{r - v_t t}{2\sqrt{at}} \right) + \exp \left( \frac{v_t r}{2a} \right) \operatorname{erfc} \left( \frac{r + v_t t}{2\sqrt{at}} \right) \right] \quad (9)$$

$$r(\mathbf{x}, \mathbf{x}') = \sqrt{(x-x')^2 + (y-y')^2 + (z-z')^2} \quad (10)$$

The dimensionless temperature  $\theta_c$  is also given by [21]:

$$\begin{aligned} \theta_c(\mathbf{X}, \mathbf{X}', F_o, Pe) &= \vartheta_c \frac{\lambda_p}{q_L} \\ &= \frac{1}{2\pi} \exp \left[ \frac{Pe}{2} X \right] \left[ \int_0^1 J(\mathbf{X}, \mathbf{X}', F_o, Pe) dZ' - \int_{-1}^0 J(\mathbf{X}, \mathbf{X}', F_o, Pe) dZ' \right] \end{aligned} \quad (11)$$

$$J(\mathbf{X}, \mathbf{X}', F_o, Pe) = \frac{1}{4R} \left[ \exp \left( -\frac{Pe}{2} R \right) \operatorname{erfc} \left( \frac{R - PeF_o}{2\sqrt{F_o}} \right) + \exp \left( \frac{Pe}{2} R \right) \operatorname{erfc} \left( \frac{R + PeF_o}{2\sqrt{F_o}} \right) \right] \quad (12)$$

$$R(\mathbf{X}, \mathbf{X}') = \sqrt{(X-X')^2 + (Y-Y')^2 + (Z-Z')^2} \quad (13)$$

where  $Pe = \frac{v_t z^*}{\alpha}$  is the Péclet number,  $\mathbf{X} = (X, Y, Z) = \frac{1}{z^*}(x, y, z)$ ,  $\mathbf{X}' = (X', Y', Z') = \frac{1}{z^*}(x', y', z')$  and  $z^*$  is any characteristic length.

To simulate the effect of prescribed time-dependent top boundary temperature  $\varphi(t)$  over an infinite plane, Eq. (3) can be simplified as follows [13]:

$$\vartheta_{tb}(z, t) = \frac{z}{2\sqrt{\pi a}} \int_0^t \frac{\varphi(\tau)}{(t-\tau)^{3/2}} \exp \left[ -\frac{z^2}{4a(t-\tau)} \right] d\tau \quad (14)$$

Moreover, if the function  $\varphi(\tau)$  is defined as

$$\varphi(\tau) = \varphi_{lu}(\tau, b_1, b_2, T_m) = T_m \left[ b_1 + b_2 \cos \left( 2\pi \left( \frac{\tau}{t_o} + L \right) \right) \right] \quad (15)$$

and with the change of variable  $u = \frac{z^2}{4a(t-\tau)}$ , the dimensionless form of Eq. (14) is

$$\begin{aligned} \theta_{tb}(F_o, F_o^w, b_1, b_2) &= \frac{\vartheta_{tb}}{T_m} \\ &= \frac{1}{\sqrt{\pi}} \int_{\frac{1}{4F_o}}^{\infty} \left[ b_1 + b_2 \cos \left( \frac{1}{F_o^w} \left( F_o - \frac{1}{4u} \right) + 2\pi L \right) \right] \frac{\exp(-u)}{\sqrt{u}} du \end{aligned} \quad (16)$$

where  $F_o^w = \frac{a}{\omega z^2}$ , with  $\omega = \frac{2\pi}{t_o}$ .

We suggest a top boundary formulation that is capable to quantify the effects of spatially variable land use in urban environments. For this, we consider the top boundary as a rectangular area within the coordinates  $[x_a, x_b]$  and  $[y_a, y_b]$ , centered in the origin, with temperature  $\varphi(t)$  surrounded by an infinite plane with zero temperature. Under these conditions, the triple integral shown in Eq. (3) can be written as

$$\begin{aligned} \vartheta_{tb}(\mathbf{x}, t) &= \frac{z}{8(\pi a)^{3/2}} \int_0^t \left\{ \frac{\varphi(\tau)}{(t-\tau)^{5/2}} \exp \left[ -\frac{z^2}{4a(t-\tau)} \right] \right. \\ &\quad \left. \int_{x_a}^{x_b} \exp \left[ -\frac{(x-x')^2}{4a(t-\tau)} \right] dx' \int_{y_a}^{y_b} \exp \left[ -\frac{(y-y')^2}{4a(t-\tau)} \right] dy' \right\} d\tau \end{aligned} \quad (17)$$

Evaluating the inner integrals, Eq. (17) simplifies to

$$\begin{aligned} \vartheta_{tb}(\mathbf{x}, t) &= \frac{z}{8(\pi a)^{1/2}} \int_0^t \frac{\varphi(\tau)}{(t-\tau)^{3/2}} \exp \left( -\frac{z^2}{4a(t-\tau)} \right) \\ &\quad \times \left[ \operatorname{erf} \left( \frac{y-y_b}{2\sqrt{a(t-\tau)}} \right) - \operatorname{erf} \left( \frac{y-y_a}{2\sqrt{a(t-\tau)}} \right) \right] \\ &\quad \times \left[ \operatorname{erf} \left( \frac{x-x_b}{2\sqrt{a(t-\tau)}} \right) - \operatorname{erf} \left( \frac{x-x_a}{2\sqrt{a(t-\tau)}} \right) \right] d\tau \end{aligned} \quad (18)$$

Including the effective heat transport velocity  $v_t$  the previous equation takes the form:

$$\begin{aligned} \vartheta_{tb}(\mathbf{x}, t) &= \frac{1}{4\sqrt{\pi}} \int_{\frac{z^2}{4at}}^{\infty} \frac{\varphi \left( t - \frac{z^2}{4au} \right)}{\sqrt{u}} \\ &\quad \times \exp(-u) \left[ \operatorname{erf} \left( \frac{Y-Y_b}{Z} \sqrt{u} \right) - \operatorname{erf} \left( \frac{Y-Y_a}{Z} \sqrt{u} \right) \right] \\ &\quad \times \left[ \operatorname{erf} \left( \frac{X-X_b}{Z} \sqrt{u} - \frac{v_t Z}{4a\sqrt{u}} \right) - \operatorname{erf} \left( \frac{X-X_a}{Z} \sqrt{u} - \frac{v_t Z}{4a\sqrt{u}} \right) \right] du \end{aligned} \quad (19)$$

The dimensionless form of Eq. (19) with  $\varphi(\tau)$  defined as Eq. (15) reads:

$$\begin{aligned} \theta_{tb}(F_o, F_o^w, Pe, \mathbf{X}, b_1, b_2) &= \frac{\vartheta_{tb}}{T_m} \\ &= \frac{1}{4\sqrt{\pi}} \int_{\frac{1}{4F_o}}^{\infty} \vartheta(F_o, F_o^w, b_1, b_2, u) \\ &\quad \times \left[ \operatorname{erf} \left( \frac{Y-Y_b}{Z} \sqrt{u} \right) - \operatorname{erf} \left( \frac{Y-Y_a}{Z} \sqrt{u} \right) \right] \\ &\quad \times \left[ \operatorname{erf} \left( \frac{X-X_b}{Z} \sqrt{u} - \frac{ZPe}{4\sqrt{u}} \right) \right. \\ &\quad \left. - \operatorname{erf} \left( \frac{X-X_a}{Z} \sqrt{u} - \frac{ZPe}{4\sqrt{u}} \right) \right] \frac{\exp(-u)}{\sqrt{u}} du \end{aligned} \quad (20)$$

where

$$\theta(F_o, F_o^w, b_1, b_2, u) = b_1 + b_2 \cos\left(\frac{1}{F_o^w} \left(F_o - \frac{1}{4u}\right) + 2\pi L\right) \quad (21)$$

and  $(X_a, X_b, Y_a, Y_b) = \frac{1}{z}(x_a, x_b, y_a, y_b)$ .

Finally, the dimensionless form of Eq. (1) is given by:

$$\theta(F_o, F_o^w, Pe, \mathbf{X}, \mathbf{X}', b_1, b_2) = \theta_o + \theta_c + \theta_{tb} \quad (22)$$

The obtained analytical approach accounts for complex, time-dependent land use effects and groundwater flow during BHE operation. In order to test its suitability for fast and flexible BHE simulation, it needs to be compared to established methods and data, such as numerical modeling or field measurements. The results from numerical verification, sensitivity analyses, and validation to experimental data are presented in the following chapter.

### 3. Results

#### 3.1. Verification

The new solution, which is formulated as Eq. (1), incorporating  $\theta_{tb}$  as defined in Eq. (19), accounts for the effects of spatially variable land use. For the verification of the analytical model, a synthetic test case is designed with four different areas of sod, bare soil, asphalt and building (Fig. 2). The temperatures for each land use are assumed to be seasonally variable and described by scaled periodic functions. These functions are parameterized according to Eq. (15), where  $L$  denotes the phase shift, and the mean temperature and the amplitude are given through the products  $b_1 \cdot T_m$  and  $b_2 \cdot T_m$ , respectively, with  $T_m$  being any given reference temperature (Table 1). These parameters are specified according to Taylor and Stefan [40], with lowest mean temperatures for sod (10.1 °C) and highest ones for the built-up area (23.2 °C). In contrast, seasonal variability is lowest in the built-up area ( $\pm 8.6$  °C), where the influence from atmospheric temperature variations is buffered. Solar radiation has strongest influence on the asphalt, and this is reflected by the relatively high amplitude of  $\pm 18.6$  °C. From the values given by [40], the mean temperature for build-up areas can be judged as a high and in comparison to other studies (e.g. [38]) extreme case. It may be interpreted as representative for specific conditions in the United States, where pronounced heat loss from non-isolated basements is observed. In their study on the city of Karlsruhe in Germany, [38] assume a mean value representative for built-up areas that is around 6 K smaller. This highlights that, even if a general framework is adopted in the following analyses, the selected scenarios are based on case-specific measurements.

The initial and top boundary conditions are represented by superimposed functions (A–F) in the analytical formulation, which

**Table 1**

Top boundary temperature parameters according to Eq. (15).

| Surface type | $b_2$ | $b_1$ | Phase shift $L$ | Reference temperature $T_m$ (°C) | Mean temperature $b_1 \cdot T_m$ (°C) | Temperature amplitude $b_2 \cdot T_m$ (°C) |
|--------------|-------|-------|-----------------|----------------------------------|---------------------------------------|--|
| Sod          | 1.3   | 1.0   | 0.4             | 10.1                             | 10.1                                  | 13.1                                       |
| Bare soil    | 1.5   | 1.0   | 0.4             | 10.1                             | 10.4                                  | 15.3                                       |
| Asphalt      | 1.8   | 1.3   | 0.4             | 10.1                             | 13.2                                  | 18.6                                       |
| Building     | 0.9   | 2.3   | 0.3             | 10.1                             | 23.2                                  | 8.6  |

are listed in Table 2. As initial conditions and “undisturbed” reference (A), it is assumed that the ground surface temperature ( $T_s$ ) equals the mean temperature for sod (10.1 °C), and that a typical and average geothermal gradient of  $0.03$  °C  $m^{-1}$  prevails. Embedded in the sod (C), rectangular areas of asphalt (D) and bare soil (E) are defined. The analytical approach allows simulating sudden changes in land use. This is considered for the component that describes construction of new buildings (F): A square area of  $50\text{ m} \times 50\text{ m}$  changes its use from bare soil to built-up from the 6th year on.

The BHE (B) is simulated through Eq. (8) with a length  $H = 50\text{ m}$  and an average heat extraction rate  $q_L = 40\text{ W m}^{-1}$ . The period of operation starts in the 12th and lasts until the 30th year. The BHE is located centrally at the fringe, between bare soil and the built-up area. The ground, which represent typical conditions of sandy aquifer [11], is assumed to be homogeneous with porosity of  $n_e = 0.25$ , volumetric heat capacity of water  $c_w = 4.2\text{ MJ K}^{-1}\text{ m}^{-3}$  and of solid  $c_s = 2.20\text{ MJ K}^{-1}\text{ m}^{-3}$ , and groundwater Darcy velocity of  $q_d = 1 \times 10^{-7}\text{ m s}^{-1}$ . The corresponding bulk properties of the porous medium are calculated following a porosity-weighted arithmetic mean [52].

The verification of the obtained analytical solution is performed by comparison with a numerical heat transport model. For this purpose, the configuration depicted in Fig. 2 is implemented in the finite element code FEFLOW (Version 6.2). In order to minimize interaction with side and bottom boundaries, a rather large numerical domain size of  $450\text{ m}$  in groundwater flow direction, of  $250\text{ m}$  width and of  $150\text{ m}$  vertical extension is chosen. It is vertically discretized by 110 layers with  $0.5\text{ m}$  thickness for the top 55 m of the aquifer, 45 layers with  $1.0\text{ m}$  thickness between 55 m and 100 m depth, and 25 layers with  $2\text{ m}$  thickness at the bottom between 100 m and 150 m depth. The BHE is represented by 111 nodal sources distributed over the top 50 m of the aquifer. The time-dependent top boundary temperature functions (C–F, Table 2) are approximated by piecewise linear functions.

The comparison of the numerical and analytical results is shown through the vertical profiles in Fig. 3. These profiles are taken at four arbitrary time points,  $t = 4.1\text{ y}$ ,  $9.6\text{ y}$ ,  $14.9\text{ y}$  and  $25.3\text{ y}$ , and at the locations P1 and P2 as indicated in Fig. 2. These locations

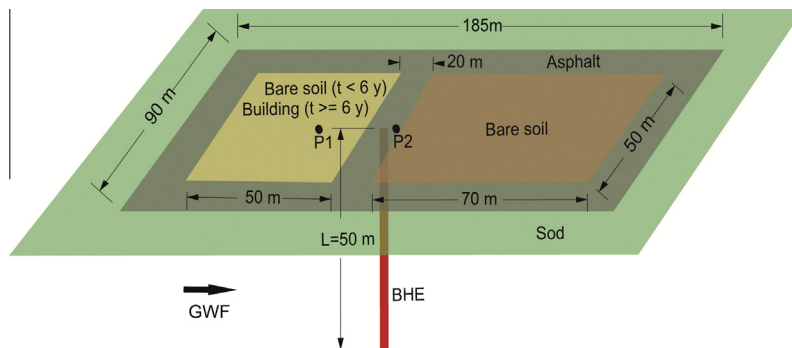


**Fig. 2.** Model setup for the numerical verification (GWf: groundwater flow).

**Table 2**  
Superpositioning functions for the numerical verification model to describe different land use types (Fig. 2).

| Superimposed function | Function type                                 | Equation | Parameters  | Time period [years] | Location of the distributed sources                   |
|-----------------------|---|----------|---|---------------------|---|
| A                     | Initial conditions                            | (6)      | $T_s = 10.1 \text{ }^\circ\text{C}$ , $k = 0.03 \text{ }^\circ\text{C m}^{-1}$                          | 0–30                | Entire half-space                                     |
| B                     | Continuous sources (MFLS)                     | (8)      | $q_L = -40 \text{ W m}^{-1}$ , $H = 50 \text{ m}$   | 12–30               | $0 \leq z \leq H$                                     |
| C                     | Top boundary: infinite plane covered with sod | (14)     | $\varphi(\tau) = \varphi_{(\text{sod})}(\tau, b_1, b_2)$  | 0–30                | Entire top boundary surface                           |
| D                     | Top boundary: area covered with asphalt       | (19)     | $\varphi(\tau) = \varphi_{(\text{asphalt})}(\tau, b_1, b_2) - \varphi_{(\text{sod})}(\tau, b_1, b_2)$   | 0–30                | Outer rectangular area (185 m × 90 m)                 |
| E                     | Top boundary: area covered with bare soil     | (19)     | $\varphi(\tau) = \varphi_{(\text{bare})}(\tau, b_1, b_2) - \varphi_{(\text{asphalt})}(\tau, b_1, b_2)$  | 0–30                | Inner rectangular areas (50 m × 50 m and 70 m × 50 m) |
| F                     | Top boundary: area covered with buildings     | (19)     | $\varphi(\tau) = \varphi_{(\text{building})}(\tau, b_1, b_2) - \varphi_{(\text{bare})}(\tau, b_1, b_2)$ | 6–30                | Inner rectangular area on the left (50 m × 50 m)      |

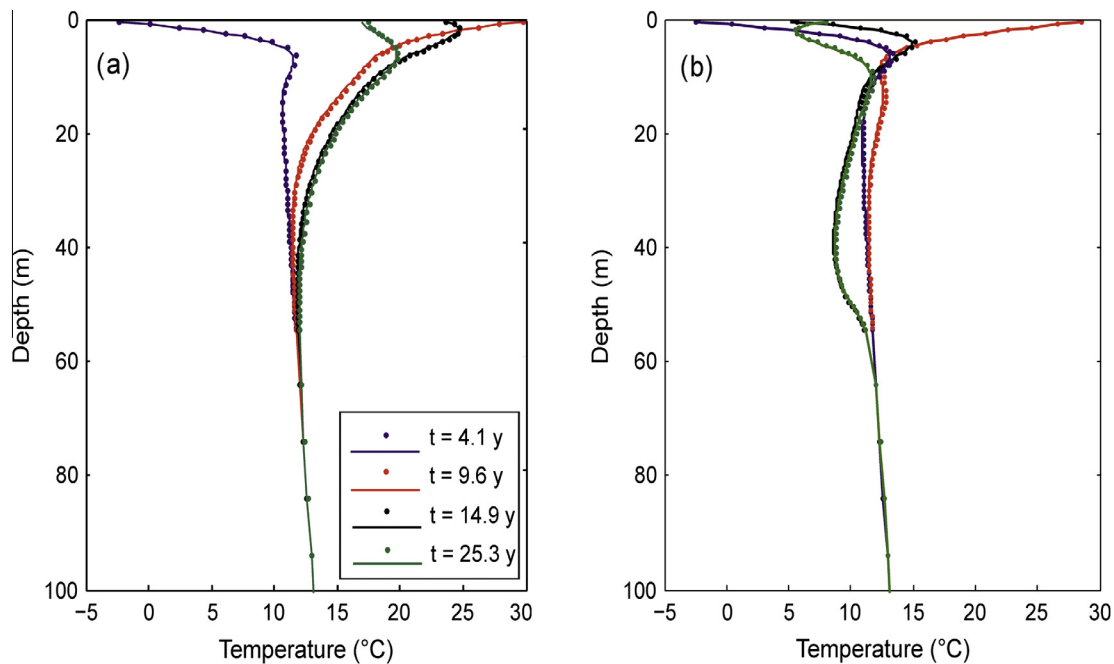


**Fig. 3.** Comparison of numerical (dots) and analytical results (continuous line): The vertical profiles are taken through the points (a) P1, located at 24 m upstream of the BHE and (b) P2, located 4 m downstream of the BHE as illustrated in Fig. 2.

are chosen along the upstream and downstream direction of groundwater flow. The one in the upstream (P1) is in the area, where abrupt temporal change of land use type, from bare soil to buildings, is simulated. The downstream monitoring point (P2) is used to inspect the performance of the simulation under the influence of the BHE and the interaction of multiple land uses.

These results confirm that the proposed analytical approach is a valuable tool for studying the thermal effect of complex and long-term changes of land use when groundwater flow is present. The root mean squared error between the numerical and the analytical solutions yields maximum values of around  $0.1 \text{ }^\circ\text{C}$ . This value is expected to decrease with finer domain discretization in the numerical model and with better degree of approximation of the time-dependent temperature in the top boundary. Note that when inspecting numerical and analytical simulations in close vicinity of the BHE, credible results from the numerical model can only be achieved by high discretization, and also the applicability of the line source for modeling the thermal effects of a BHE here is limited [53].

### 3.2. Influence of changing land use and groundwater flow

The analytical model facilitates a rigorous sensitivity analysis of the thermal effects of land use and groundwater flow. For

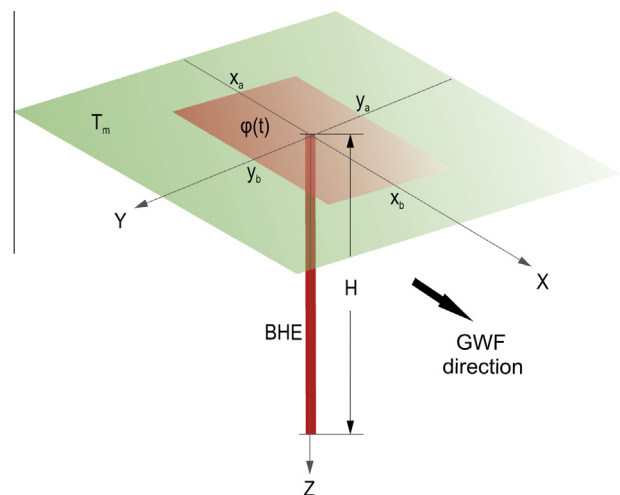


**Fig. 4.** Model setup for the dimensional analysis. The finite plane (red square) within the coordinates  $[x_a, x_b]$  and  $[y_a, y_b]$  represents a sudden change in temperature  $\varphi(t)$  respect to the background conditions given by the mean reference temperature  $T_m$ . (For interpretation of the references to colour in this figure legend, the reader is referred to the web version of this article.)

generalization, this is carried out in a dimensional analysis with a streamlined variant of the scenario shown in Fig. 2. This variant is depicted in Fig. 4 and considers two different land use types. A square area with a distinctive land use is defined at the center of the domain. The length of the square area and the length of the BHE are assumed to be equal ( $x_b - x_a = y_b - y_a = H = 50$  m), in the following, this length constitutes the characteristic length ( $z^*$ ) for the dimensionless numbers. The square represents a sudden change in land use (such as a new building with a GSHP inside) and is simulated by a finite plane with a different temperature than the superpositioned infinite plane (background). The operation of the BHE is assumed to start simultaneously with this land cover change.

The temperature of the infinite plane  $T_m = 10.1$  °C represents the mean temperature of sod (Table 1). This temperature is assumed to be constant and equal to the initial temperature in the whole domain. In the red square, the temperature is set seasonally variable (Fig. 4). Here we simulate asphalt and/or built-up area, which are implemented by adjusting the parameters  $b_1$  and  $b_2$  in Eq. (15) according to the values shown in Table 1.

In order to quantify the net effect of the square, the background temperature is subtracted from the entire top boundary solution  $\theta_{tb}$ . Thus, this becomes:

$$\begin{aligned} \theta_{tb}(F_o, F_o^w, Pe, \mathbf{X}, b_1, b_2) &= \frac{\vartheta_{tb}}{T_m} \\ &= \frac{1}{4\sqrt{\pi}} \int_{\frac{y}{z}}^{\infty} \{4\vartheta(F_o, F_o^w, b_1, b_2, u) \\ &+ [\vartheta(F_o, F_o^w, b_1, b_2, u) - 1] \\ &\times [\operatorname{erf}\left(\frac{Y - Y_b}{Z} \sqrt{u}\right) - \operatorname{erf}\left(\frac{Y - Y_a}{Z} \sqrt{u}\right)] \\ &\times \left[ \operatorname{erf}\left(\frac{X - X_b}{Z} \sqrt{u} - \frac{ZPe}{4\sqrt{u}}\right) \right. \\ &\left. - \operatorname{erf}\left(\frac{X - X_a}{Z} \sqrt{u} - \frac{ZPe}{4\sqrt{u}}\right) \right] \} \frac{\exp(-u)}{\sqrt{u}} du - 1 \quad (23) \end{aligned}$$

Finally, since the BHE is simulated with the MFLS, the dimensionless ratio  $\frac{q_b}{z^* T_m}$  is assumed constant so that Eqs. (23) and (11) are in a comparable form within the entire solution of dimensionless temperature,  $\theta$ .

Contours of dimensionless temperature are depicted at two different planes in Fig. 5, where coordinates are given in non-dimensional form. Here,  $\theta$  is compared with the MFLS to highlight the influence from the square in the top boundary, which is assumed to be covered with buildings. The shown temperatures are calculated at  $F_o = 0.6$ , which corresponds to 50 years of operation. A constant groundwater flow (GWF) velocity with  $Pe = 5.0$  ( $q_d = 1.8$  m/y) is assumed, upstream direction of groundwater flow is specified by negative  $X$ , whereas positive  $X$  denotes downstream direction. Thus, the BHE is located at the origin and is aligned with  $Z$ .

Fig. 5(a) shows the dimensionless temperature at the horizontal plane  $Z = 0.5$  for the half-space  $Y \geq 0$ . The figure indicates that the vertical heat flux from the square on the top boundary generally overprints the temperature drop induced by the BHE. In fact, when a built-up area exists, negative dimensionless temperatures  $\theta$  are restricted to a narrow domain around the borehole. Moreover,  $\theta$  does not show a monotonic behavior, since a maximum value can be identified between  $X = 0.25$  and  $X = 1$  at  $Y = 0$ . This maximum marks the point where the temperature is driven either by the BHE (upstream) or the downstream end of the built-up area. Clearly, this maximum is also affected by the direction and magnitude of groundwater flow.

Fig. 5(b) shows a cross sectional view and features the strong influence of the horizontal and vertical thermal gradients

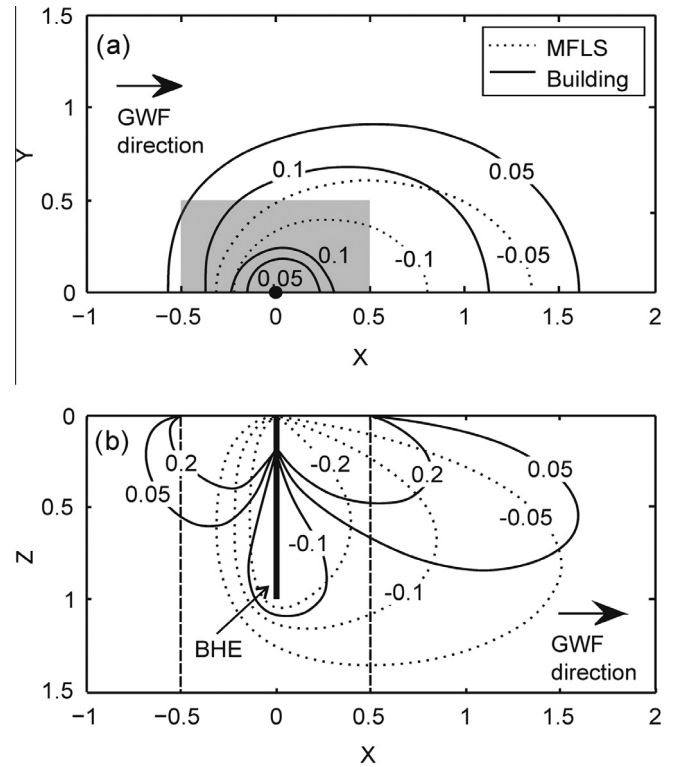
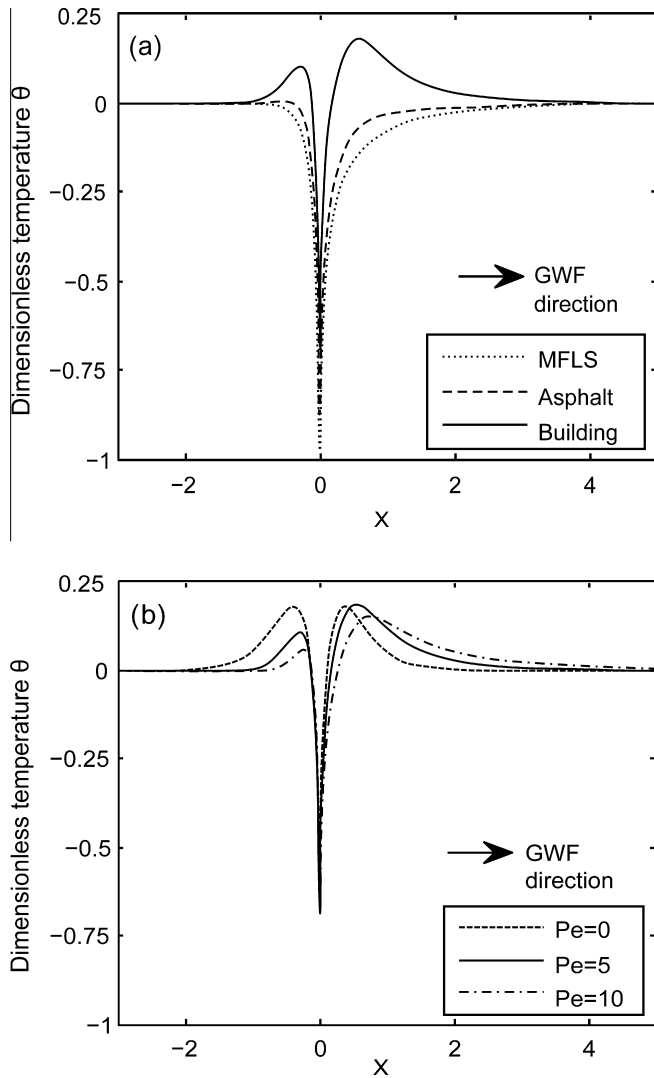


Fig. 5. Dimensionless temperature contours for  $F_o = 0.6$  and  $Pe = 5.0$  at: (a) the horizontal plane  $Z = 0.5$ , the changing land use area is projected in gray (b) the vertical plane  $Y = 0$ , the vertical dashed lines indicate the limits of the changing land use area; MFLS: moving finite line source, GWF: groundwater flow.

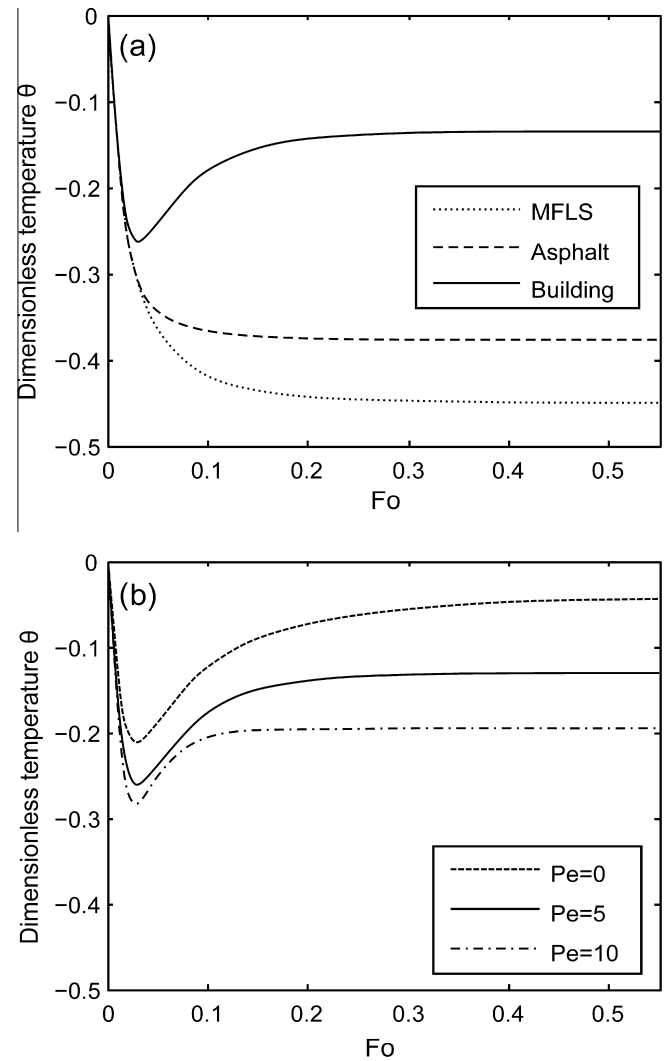
associated with the finite plane on top. As expected, the boundary effect is enhanced downstream by groundwater flow and diminishes with depth. Nonetheless, it can be seen even below the toe of the borehole. At these depths ( $Z > 1.0$ ), the MFLS estimates a maximum temperature decrease by around 2 K (i.e. a dimensionless  $\theta = -0.2$ ), however, by including a different top boundary (e.g. building) it is only around 1 K. Hence, the new building, i.e. a change in land use type, partially compensates the temperature decrease, which is triggered by the BHE. This result confirms the key role of land use variability and groundwater flow on the long-term temperature response. It also highlights the relevance of these factors for appropriate and optimized BHE design in particularly in densely and newly build-up areas, where the BHE is close to buildings or integrated in the slab (foundation) of the building as proposed, for example by Zhang et al. [54].

Fig. 6 depicts the computed dimensionless temperature  $\theta$  as a function of dimensionless horizontal distance  $X$  from the line source. Again, a moderate, constant groundwater flow velocity ( $Pe = 5.0$ ) is selected for Fig. 6(a), and the impact from different land use types is compared. The simulation time is kept at  $F_o = 0.6$ . The existing moving line source solution (MFLS), which does not account for top boundary effects, serves again as reference.

The BHE induces a decrease of the ground temperature, which is most pronounced close to the line source ( $X = 0$ ). By considering the heat flux from the top boundary, the generated energy deficit is (partially) replenished. In the case of asphalt, temperatures close to the initial state are obtained for a downstream distance of more than  $x = 1.5 H$ . For a built-up area, even higher temperatures than the initial ones are obtained close to the borehole. For the studied case, a maximum dimensionless temperature of 0.18 is computed, which corresponds to a temperature of 1.8 K higher than in the surrounding environment. As expected, the length of the thermal



**Fig. 6.** Length of thermal disturbance at dimensionless time  $F_o = 0.6$  and  $Y = 0$ ,  $Z = 0.5$  under: (a) changing land use with Péclet number  $Pe = 5.0$  and (b) different values of  $Pe$  for a built-up area (see Table 1); MFLS: moving finite line source; GWF: groundwater flow.



**Fig. 7.** Temperature response over dimensionless time  $F_o$  at  $X = 0.1$ ,  $Y = 0$ ,  $Z = 0.5$  under: (a) different land use types with Péclet number  $Pe = 5.0$ , and (b) different values of  $Pe$  for a built-up area (see Table 1); MFLS stands for moving finite line source.

anomaly increases with the thermal intensity of the top boundary. It reaches relative values of up to four times the length of the borehole on the downstream side for the built-up area. Fig. 6(b) shows the influence of the different groundwater flow velocity on the heat transport from buildings. It is demonstrated how horizontal advection enhances the asymmetry of dimensionless temperature,  $\theta$ . Groundwater advection, however, also mitigates the peak thermal disturbance, which declines from  $\theta = 0.18$  to  $0.15$  in the downstream direction. Furthermore, the results demonstrate that for the specific case the top boundary, i.e. land use, appears to be more important for the heat dissipation of a BHE than the groundwater advection. This, however, may be different for higher GWF velocities and in case of thermally isolated foundations.

Next, we investigate the time-dependency of top boundary effects (Fig. 7). Again, the MFLS is selected as reference and land use in the central square is assumed to be asphalt or building (Fig. 4). Fig. 7(a) shows the simulated dimensionless temperature trends for the scenario with groundwater flow ( $Pe = 5.0$ ) in downstream direction at  $X = 0.1$  and at half the length of the BHE,  $Z = 0.5$ . The results show that the temperatures of all land use types initially follow the same trend, which is caused by the rather slow propagation of heat flux from the top boundary to greater

depths, and thus the thermal effects at  $Z = 0.5$  appear delayed. The temperature obtained by the MFLS follows a hyperbolic trend and arrives at around  $F_o = 0.4$  at a (quasi-)steady state. This state is reached earlier in case of increased heat fluxes from the top boundary, such as from asphalt and buildings. The thermal anomaly does not grow as much and stabilizes at around  $F_o = 0.3$ .

Higher heat fluxes from built-up areas yield characteristic transient behaviors (Fig. 7). After initial cooling from BHE operation, the thermal front reaches the examined depth at  $Z = 0.5$  and heats the ground slightly until a steady-state is attained at around  $F_o = 0.3$ . At the studied point, the built-up area can increase the steady-state temperature induced by the operation of BHE by about  $3.2$  K ( $\Delta\theta = 0.32$ ). In comparison, for the case with asphalt, this increase is only  $0.7$  K ( $\Delta\theta = 0.07$ ).

In Fig. 7(b), the role of groundwater flow velocity is highlighted and the focus again is on the built-up area as top boundary. With increase of groundwater velocity, the thermal steady state is reached earlier [21] and at lower steady-state temperatures [27]. In summary, these scenarios underline that even at considerable depth, the top boundary condition can potentially have a strong and delayed impact on the temperature anomaly. Taking the MFLS solution for comparison, the discrepancies increase with

time and with the strength of the top boundary. The depth-dependency is further studied in the following.

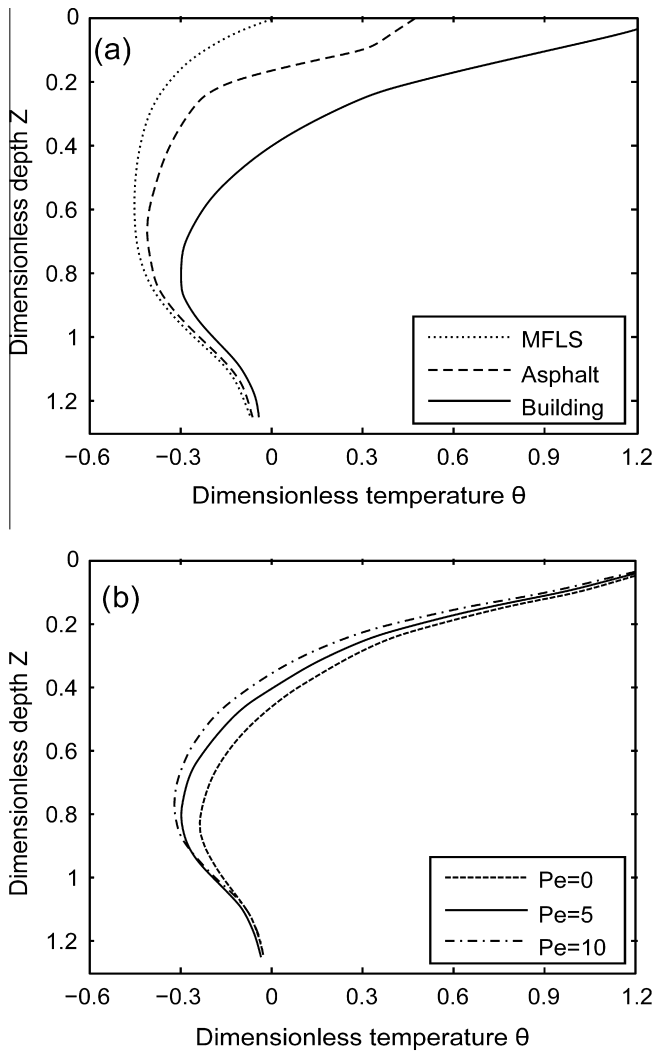


**Fig. 8.** Dimensionless temperature profiles at dimensionless time  $F_o = 0.6$  and  $X = 0.1, Y = 0$  assuming: (a) different land use types with Péclet number  $Pe = 5.0$  and (b) different values of  $Pe$  for a built-up area (see Table 1); MFLS: moving finite line source.

Fig. 8 depicts the dimensionless temperature  $\theta$  as a function of dimensionless depth,  $Z$ , assuming the same study case as above in Fig. 4. We focus on late time, (quasi-)steady-state conditions ( $F_o = 0.6$ , or equivalently 50 years of operation). As illustrated in Fig. 8(a), the MFLS provides a vertically variable temperature profile. However, a crucial assumption for the MFLS is that the top boundary temperature is equal to the initial temperature in the model domain. This assumption can be considered as appropriate for conditions without significant land use influence or as static approximation for transient land use effects. The two different land use scenarios with asphalt and building show how thermal anomalies induced by BHEs are strongly influenced by the strength of the top boundary. This thermal influence can be seen not only in shallow depths. For instance, at the borehole toe, the heat flux from the built-up area increases the temperature by about 0.6 K ( $\Delta\theta = 0.06$ ). In comparison, the influence from asphalted area is negligible at this depth. Under steady-state conditions ( $F_o \geq 0.6$ ), the high heat flux from buildings can overcome the drop in temperature induced by the MFLS until a depth of approximately 0.4 H. Covering the surface with asphalt compensates the heat deficit until a depth of approximately 0.2 H. Thus, the type of land use defines the minimum temperature and also the penetration depth.

The role of different groundwater velocities is studied in Fig. 8(b), selecting the same downstream distance from the BHE as for the profiles in Fig. 8(a) ( $x = 0.1 H$ ). As expected, higher groundwater velocities and, therefore, higher advective heat flux, yields generally lower temperatures. This is due to the faster downstream migration of the cold plume induced by the BHE (e.g. [55]). Advection therefore mitigates the evolving thermal plume, and this is most visible in axial direction with minor influence of the  $Pe$  number close to the top boundary and at the borehole toe.

### 3.3. Application to the Elgg field site

There are only few sites, where the long-term evolution of ground temperatures has been monitored in the close vicinity of BHEs [11]. An exemption is a GSHP system close to Zurich, Switzerland. Since 1986, a single coaxial GSHP with 105 m length and a heat extraction rate of up of  $70 \text{ W m}^{-1}$  has been supplying heating to a single house in the rural area of the municipality of Elgg. During repeated measurement campaigns from 1986 to 1998, depth-dependent ground temperatures were recorded. A detailed description of the site can be found in [56]. We utilize this case study for validating the applicability of the proposed

**Table 3**  
Vertical geological profile at the Elgg site [56].

| Depth $z$ (m) | $\Delta z$ (m) | Material       | $\rho$ ( $\text{kg m}^{-3}$ ) | $\lambda_p$ ( $\text{W m}^{-1} \text{K}^{-1}$ ) | $C_p$ ( $\text{J kg}^{-1} \text{K}^{-1}$ ) |
|---------------|----------------|----------------|-------------------------------|---|--|
| 0.00          |                |                |                               |   |  |
| 2.25          | 2.25           | Ground surface | 2700                          | 3.5   | 800  |
| 11.25         | 9.00           | Conglomerate   |                               | 3.7   | 1600                                       |
| 18.75         | 7.50           | Marl           |                               | 3.0   | 800  |
| 21.25         | 2.50           | Conglomerate   |                               | 3.4   | 1200                                       |
| 36.75         | 15.50          | Marl           |                               | 3.0   | 800  |
| 40.25         | 3.50           | Sandstone      |                               | 4.0   | 800  |
| 63.25         | 23.00          | Marl           |                               | 3.0   | 800  |
| 66.75         | 3.50           | Conglomerate   |                               | 3.7   | 1600                                       |
| 75.00         | 8.25           | Marl           |                               | 3.0   | 800  |
| 79.25         | 4.25           | Sandstone      |                               | 4.0   | 800  |
| 83.25         | 4.00           | Marl           |                               | 3.0   | 800  |
| 86.75         | 3.50           | Sandstone      |                               | 4.0   | 800  |
| 90.00         | 3.25           | Marl           |                               | 3.0   | 800  |
| 93.50         | 3.50           | Sandstone      |                               | 4.0   | 800  |
| 97.00         | 3.50           | Marl           |                               | 3.0   | 800  |
| 102.00        | 5.00           | Sandstone      |                               | 4.0   | 800  |
| 130.00        | 28.00          | Marl           |                               | 3.0   | 800  |

analytical approach. Since groundwater effects have not been detected at the site, no groundwater flow is considered for the model calibration. Instead, the potential role of horizontal groundwater advection is subsequently examined.

A simplified lithological profile at the Elgg site is provided in Table 3 [56]. It consists of a sedimentary setting with alternate layers of sandstones, marlstones and conglomerates. The thermal properties of these materials indicate rather uniform values with thermal conductivities ranging between 3.0 and 4.0 W m<sup>-1</sup> K<sup>-1</sup>. This range fits well within literature values reported for the similar sedimentary rocks [57].

The measured temperature-depth-profiles (TDPs) are dominated by a geothermal gradient of 0.03 °C/m (Fig. 9), however, the point at which these profiles deviate from the geothermal gradient seems to be located at greater depths for later times [6]. The mean ground surface temperature ( $T_s$ ) can be estimated by taking the TDP for December 1986 in Fig. 9, which is the initial TDP without any influence from the BHE (Fig. 9, red dots), and extending the trend defined by the geothermal gradient until the ground surface. In this way, the approximated mean  $T_s$  is 9 °C.

At the site, long-term subsurface temperature data has been recorded at two observation wells located at 1 m and 0.5 m distance from the BHE, respectively. In total, 10 sensors ( $\pm 0.1$  K accuracy,  $\pm 0.001$  K precision) were installed at each well and at

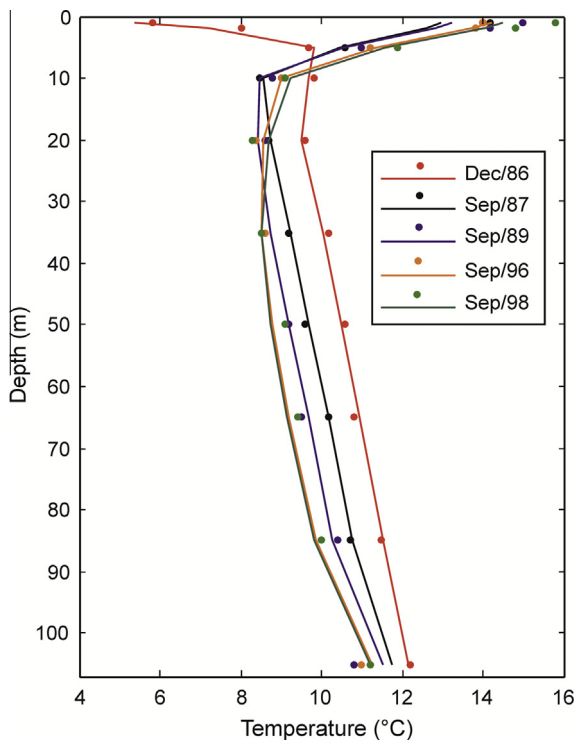


Fig. 9. Temperature-depth profiles (TDPs) obtained from the repeated measurements (dots) and calculated (continuous lines) with the analytical solution at 1 m distance from the BHE at the Elgg site.

different depths along the entire BHE length [6]. Additionally, the heat pump is equipped with a monitoring system that records the time series of temperature change in the inner fluid circulating through the coaxial BHE and also the energy output from the installation. These data are available for the heating period of 1990–1991 [56], when the heat extraction rate varied between 50 W m<sup>-1</sup> and 70 W m<sup>-1</sup>. For the same period, the number of operational hours shows a high variability starting with 75 h in October 1990 and finishing with 132 h in April 1991, with a maximum of 357 h in February 1991.

The application of the proposed analytical solution to this study case requires defining an equivalent homogenous porous medium as a surrogate of actual layered geological setting. The thermal properties of this equivalent porous medium are found during the model calibration. Furthermore, accurate simulation of the GSHP system requires a detailed knowledge of its load profile. This profile defines the amount of energy that should be extracted from the subsurface in order to satisfy a specific space-heating demand. Here, the profile is approximated as a function of heat extraction rate and the recorded operational time of the system. For the former, a constant heat rate of 60 W m<sup>-1</sup> is assumed, which is the mean value of the known rates for the heating period of 1990–1991. Since the number of operational hours shows a clear seasonal dependency, the temporal variability is approximated by a periodic function whose mean, amplitude and phase-shift are also calibrated. In this manner, an equivalent heat extraction rate is obtained for each month within the entire simulation period. The MFLS solution with this time-dependent rate is formulated by temporal superposition over the variable monthly load as follows:

$$\vartheta_c(\mathbf{x}, \mathbf{x}', t) = \sum_{i=1}^N \frac{q_L^i - q_L^{i-1}}{2\pi\lambda_p} \exp\left(\frac{\nu_L \mathbf{x}}{2a}\right) \left[ \int_0^H j(\mathbf{x}, \mathbf{x}', t^N - t^i) dz' - \int_{-H}^0 j(\mathbf{x}, \mathbf{x}', t^N - t^i) dz' \right] \quad (24)$$

where the superscript  $i$  refers to the specific month and  $N$  to the total number of months.

The GSHP system is located in a suburban area potentially affected by land use changes and regional climate trends. Since it is not possible to track all changes in land use at this site, the top boundary temperature is assumed time dependent and consisting of a linear trend superposed to a calibrated annual periodic function. This simplification implies that the solution given by Eq. (19) reduces to Eq. (14) taking into account that groundwater flow is imperceptible at this site. The derived analytical solution represents superpositioning of functions A, B and C listed in Table 4.

For calibration, the measurements from the observation well located at 1 m distance from the BHE are considered during the period 1986–1991 (the first continuous measuring campaign). The data at 85 m depth is used to calculate the thermal properties of the equivalent porous medium and of the parameters of seasonal load profile. Subsequently, the measurements at 5 m depth are used to calibrate the top boundary temperature function.

The results of the validation of the analytical simulation are shown in Fig. 9. The RMSE varies between 0.18 °C and 0.70 °C, the highest values are driven by model inaccuracies close to the

Table 4  
Superpositioned analytical functions for the Elgg site.

| Superimposed function | Function type                | Equation | Parameters  | Time period [years] | Location of the distributed sources |
|-----------------------|------------------------------|----------|---|---------------------|-------------------------------------|
| A                     | Initial conditions           | (6)      | $T_s = 9$ °C, $k = 0.03$ °C m <sup>-1</sup>                               | 0–12                | Entire half-space                   |
| B                     | Continuous sources (MFLS)    | (24)     | $q_L$ = monthly (seasonally) variable heat rate                           | 0–12                | $0 \leq z \leq 105$ m               |
| C                     | Top boundary: infinite plane | (14)     | $\varphi(\tau)$ = linear trend plus a seasonal temperature with mean 9 °C | 0–12                | Infinite plane at the top boundary  |

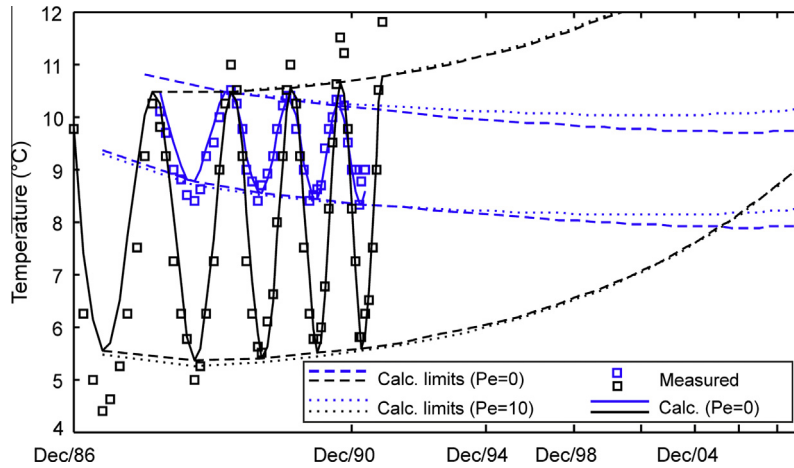


**Fig. 10.** Temperature time series at 1 m distance from the BHE at 5 m depth (black) and 85 m depth (blue) at the Elgg site. Measured data is compared with calculated values under no groundwater flow ( $Pe = 0$ ). The limits of the calculated oscillating temperature – with ( $Pe = 10$ ) and without ( $Pe = 0$ ) groundwater flow – are also shown and extended for the period after 1991, when no measurements are available. (For interpretation of the references to colour in this figure legend, the reader is referred to the web version of this article.)

BHE toe, where the influence of an underlying aquifer is not considered in the simulation.

Results shown in Fig. 9 indicate that the analytical solution is able to closely reproduce the measured ground temperatures. The good fitting includes the period of calibration (1986–1991) and the extrapolated profiles until 1998. Looking at the last two calculated profiles (Sep/96 and Sep/98), it can be concluded that a quasi-steady state has been reached in the vicinity of the borehole leading to a sustainable GSHP operation as also described in Rybach and Eugster [6]. Furthermore, the capabilities of the proposed analytical solution to reproduce the measured temperature can also be addressed by comparing the time series of temperature (measured data) at two different depths with the calculated values for  $Pe = 0$  in Fig. 10.

The calibrated thermal conductivity and volumetric heat capacity are  $3.24 \text{ W m}^{-1} \text{ K}^{-1}$  and  $2.50 \times 10^6 \text{ J m}^{-3} \text{ K}^{-1}$ , respectively. These values are comparable with the (weighted) arithmetic mean of the values shown Table 3, which are  $3.20 \text{ W m}^{-1} \text{ K}^{-1}$  and  $2.38 \times 10^6 \text{ J m}^{-3} \text{ K}^{-1}$ , respectively.

The calibrated ground surface temperature is  $T_s(t) = 9.0 + 0.15t + 7.2\sin(2\pi(t + 0.49))$ , where  $t$  is the time in years. This function indicates a linear increase of  $1.5 \text{ }^\circ\text{C/decade}$  in the  $T_s$  and is driven by the actual temperature increase of  $1.5 \text{ }^\circ\text{C}$  in four years (1987–1991) at 5 m depth, which also can be seen in the measured data (Fig. 10). According to [58], the air temperature in northern Switzerland had a trend of only  $0.38 \text{ }^\circ\text{C/decade}$  for the period 1984–2013. However, at small scales, like the single house we are considering here, site-specific GST conditions apparently play a substantial role and a coupled relation between ground surface and air temperatures is hard to establish [59,60]. It is also worth mentioning that  $T_s$  is valid only for the period of calibration. For longer periods, more detailed  $T_s$  models, however, could also be implemented [61].

Finally, the number of operational hours  $OH$  follows the function  $OH(t) = 190.37 + 172.27\sin(2\pi\frac{t}{12})$  where  $t$  is the time in months. This function yields a minimum number of operational hours of 18 h/month in July and a maximum of 363 h/month in February. The latter corresponds well with the records from 1991.

With all parameters properly calibrated, we conclude that the presented modeling framework is efficient and suitable to simulate the ground temperature effects of BHE operation. The calibration also facilitates a closer view at the top boundary influence and to quantify the transient vertical heat flux. Groundwater, however,

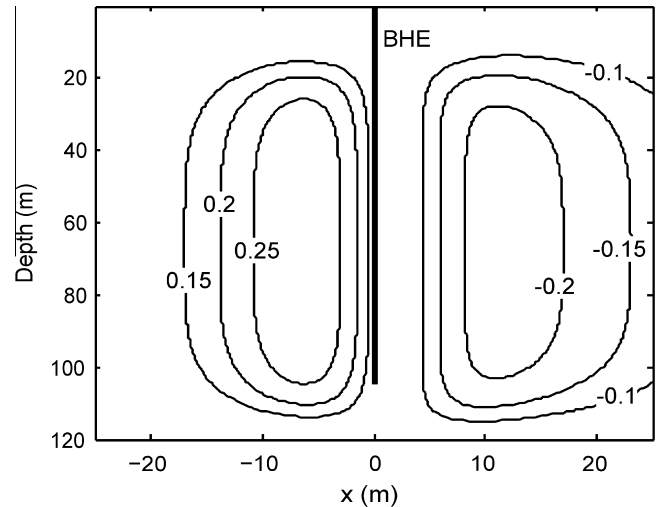


**Fig. 11.** Isolines of temperature difference  $T_{Pe=10} - T_{Pe=0}$  for the calibrated model at the Elgg site and after 48 months of operation.

is missing at the site, and this is hypothetically considered in the following analysis.

### 3.4. Groundwater flow at the Elgg site (hypothetical case)

Despite the fact that groundwater flow is negligible at the Elgg site, the easy implementation of the methodology allows to carry out an analysis of its potential role and impact. Hence, we use this field site as a reference to examine the potential influence of horizontal advection. Assuming a moderate GWF velocity ( $Pe = 10$ ,  $q_d = 2.3 \text{ m/year}$ ), a comparison of time series of temperature at two different depths ( $z = 5 \text{ m}$  and  $z = 85 \text{ m}$ ) for  $Pe = 10$  and  $Pe = 0$  (real case) is shown in Fig. 10. For simplicity in the comparison, the simulated temperature has a monthly resolution within the calibration period 1986–1991 (continuous lines), that is, the period when real data is also available. Subsequently, only the minimum and maximum temperature envelopes are shown for each  $Pe$  and depth.

Fig. 10 illustrates the dampening effect on the surface temperature amplitude at 85 m depth. At this level, the temperature is almost entirely influenced by the transient heat flux to the

BHE. Notoriously, the system converges to a thermal equilibrium after 2000. Under the presence of groundwater flow, a steady state is reached earlier and the induced steady-state temperature anomaly is less pronounced. This is alleviated by the assumption of a transient heat extraction rate, which includes recovery periods with almost zero operational hours (June–August).

At 5 m depth, a stronger influence from top boundary conditions is naturally observed, whereas the effect of groundwater flow is clearly negligible (see also Fig. 8(b)). The temperature response, and especially its lower envelope, remarkably increases as a consequence of the  $T_s$  function. As mentioned above, forecasts of temperature series outside the calibration period using this functional form may be not realistic and, therefore, we restrict our analysis to the relative role of groundwater flow.

The calculated field of temperature difference  $T_{pe=10} - T_{pe=0}$  (with – without groundwater flow) for the plane  $y = 0$  after 48 months of operation is shown in Fig. 11. Since the top boundary is only a function of time, only vertical gradients are present at the plane  $z = 0$ , leading to an insensitive  $\vartheta_{tb}$  solution to groundwater flow (see Fig. 5(b)) for comparison). As expected, groundwater flow creates an extended but less pronounced cooling effect at the downstream side.

#### 4. Conclusions

We proposed a new analytical form that considers groundwater flow and land surface effects on the ground heat transport of borehole heat exchangers (BHEs). The analytical framework is able to simulate temporal and spatial changes at the top boundary (i.e. land surface) temperature. The solution is presented to complement existing solutions, such as the moving finite line source (MFLS), in order to account for the influence of land use variability in the long-term response of a BHE. The analytical approach is successfully verified using a numerical heat transport model. For this verification, a rather complex scenario was implemented and aimed to represent, at small scale, the heterogeneity in land use typical for urban areas. The results obtained motivate the implementation of this approach for more multifaceted configurations at larger spatial (urban) scales, like the study by [54], who investigated the potential application of GSHP systems for the City of Westminster in London.

With the described analytical framework, a dimensional analysis was performed to quantify the role of different top boundary strengths and groundwater flow in the thermal anomaly induced by a BHE operation. Depending of the land use type, the heat deficit can be replenished at relatively short horizontal distance from the BHE. The top-boundary-induced heat flux propagates downwards and can reach the BHE end yielding even higher temperatures than in the initial state at depths between 0.2 and 0.4 times the BHE length. Strong groundwater flow could potentially wash out this heat flux leading to lower temperatures in depth while also creating extended and smoothed anomalies downstream. The timing of steady-state conditions is influenced by the top boundary strength and this indicates the importance of land use variability to properly design GSHP systems in urban environments.

The demonstrated application of the methodology to the Elgg site is an example of how under certain conditions a complex system can be well approximated by simplified analytical functions. It is clear that the line source model is not able to reproduce the detailed heat transfer between the ground and the inner circulating fluid within the BHE. However, our approximation with a seasonal heat transfer rate shows acceptable results without going for computational and timely expensive numerical simulations. The derived sustainable operational status, reached after around 14 years, agrees with previously published results for the same

site. This status is reached due to the axial effects included in the MFLS when groundwater flow is negligible. This condition, together with the assumption of homogeneous ground at the site, enabled a decent reproduction of measured temperatures especially at mid and greater depths. By assuming a hypothetical scenario, where the Elgg site is influenced by groundwater flow, the role of advective heat transport was analysed for field conditions. As expected, advection mitigates the thermal impact from BHE operation and accelerates steady-state conditions.

The proposed solution can be used in a variety of scenarios, in which the spatial and temporal changes in the top boundary temperature are relevant, like in BHE below buildings and in urban environments. Long-term changes in land use for instance, induce thermal anomalies that propagate in the subsurface reaching levels that could substantially improve the operation and design of shallow geothermal systems. Some practical procedures and software for designing GSHP systems (e.g. [62]) based on the superposition of analytical functions could be extended to involve top boundary effects following the proposed methodology.

#### Acknowledgements

This work was supported by the by the Swiss National Science Foundation (SNSF) under Grant Number 200021L 144288, and the German Research Foundation (DFG), under Grant Number BL 1015/4-1, and, within the GEOTHERM-II project, by the Competence Center Energy and Mobility (CCEM) and Competence Center for Environment and Sustainability (CCES) of the ETH-Domain. We thank Gabrielle Moser for language corrections.

#### References

- [1] Lund JW, Freeston DH, Boyd TL. Direct utilization of geothermal energy 2010 worldwide review. *Geothermics* 2011;40(3):159–80.
- [2] Blum P, Campillo G, Kölbl T. Techno-economic and spatial analysis of vertical ground source heat pump systems in Germany. *Energy* 2011;36(5):3002–11.
- [3] Saner D et al. Is it only CO<sub>2</sub> that matters? A life cycle perspective on shallow geothermal systems. *Renew Sustain Energy Rev* 2010;14(7):1798–813.
- [4] Galgaro A et al. Feasibility analysis of a Borehole Heat Exchanger (BHE) array to be installed in high geothermal flux area: the case of the Euganean Thermal Basin, Italy. *Renew Energy* 2015;78:93–104.
- [5] Olfman MZ, Woodbury AD, Bartley J. Effects of depth and material property variations on the ground temperature response to heating by a deep vertical ground heat exchanger in purely conductive media. *Geothermics* 2014;51:9–30.
- [6] Rybach L, Eugster WJ. Sustainability aspects of geothermal heat pump operation, with experience from Switzerland. *Geothermics* 2010;39(4):365–9.
- [7] Chen J et al. Simulation and experimental analysis of optimal buried depth of the vertical U-tube ground heat exchanger for a ground-coupled heat pump system. *Renew Energy* 2015;73:46–54.
- [8] Vienken T et al. Sustainable intensive thermal use of the shallow subsurface—a critical view on the status quo. *Groundwater* 2014. <http://dx.doi.org/10.1111/gwat.12206>.
- [9] Haehnlein S, Bayer P, Blum P. International legal status of the use of shallow geothermal energy. *Renew Sustain Energy Rev* 2010;14(9):2611–25.
- [10] Butscher C et al. Risikoorientierte Bewilligung von Erdwärmesonden. *Grundwasser* 2011;16(1):13–24.
- [11] Stauffer F et al. *Thermal use of shallow groundwater*. CRC Press; 2013.
- [12] Beier RA. Transient heat transfer in a U-tube borehole heat exchanger. *Appl Therm Eng* 2014;62(1):256–66.
- [13] Carslaw H, Jaeger J. *Conduction of heat in solids*. second ed. New York: Oxford University Press; 1959.
- [14] Eskilsson P. Thermal analysis of heat extraction boreholes. Ph.D. Thesis, University of Lund, Lund, Sweden; 1987.
- [15] Kim E-J et al. A hybrid reduced model for borehole heat exchangers over different time-scales and regions. *Energy* 2014;77:318–26.
- [16] Li M et al. Full-scale temperature response function (G-function) for heat transfer by borehole ground heat exchangers (GHEs) from sub-hour to decades. *Appl Energy* 2014;136:197–205.
- [17] Zeng H, Diao N, Fang Z. A finite line-source model for boreholes in geothermal heat exchangers. *Heat Transf – Asian Res* 2002;31(7):558–67.
- [18] Lamarche L, Beauchamp B. A new contribution to the finite line-source model for geothermal boreholes. *Energy Build* 2007;39(2):188–98.
- [19] Sutton MG, Nutter DW, Couvillion RJ. A ground resistance for vertical bore heat exchangers with groundwater flow. *J Energy Resour Technol* 2003;125(3):183–9.

- [20] Diao N, Li Q, Fang Z. Heat transfer in ground heat exchangers with groundwater advection. *Int J Therm Sci* 2004;43(12):1203–11.
- [21] Molina-Giraldo N et al. A moving finite line source model to simulate borehole heat exchangers with groundwater advection. *Int J Therm Sci* 2011;50(12):2506–13.
- [22] Marcotte D, Pasquier P. Fast fluid and ground temperature computation for geothermal ground-loop heat exchanger systems. *Geothermics* 2008;37(6):651–65.
- [23] Hecht-Méndez J et al. Optimization of energy extraction for vertical closed-loop geothermal systems considering groundwater flow. *Energy Convers Manage* 2013;66:1–10.
- [24] García-Gil A et al. The thermal consequences of river-level variations in an urban groundwater body highly affected by groundwater heat pumps. *Sci Total Environ* 2014;485–486:575–87.
- [25] Casasso A, Sethi R. Efficiency of closed loop geothermal heat pumps: a sensitivity analysis. *Renew Energy* 2014;62:737–46.
- [26] Ferguson G. Screening for heat transport by groundwater in closed geothermal systems. *Groundwater* 2014.
- [27] Tye-Gingras M, Gosselin L. Generic ground response functions for ground exchangers in the presence of groundwater flow. *Renew Energy* 2014;72:354–66.
- [28] Beck M et al. Geometric arrangement and operation mode adjustment in low-enthalpy geothermal borehole fields for heating. *Energy* 2013;49:434–43.
- [29] Hähnlein S et al. Sustainability and policy for the thermal use of shallow geothermal energy. *Energy Policy* 2013;59:914–25.
- [30] Chiasson AD, Rees SJ, Spitzer JD. A preliminary assessment of the effects of ground-water flow on closed-loop ground-source heat pump systems. *ASHRAE Trans* 2000;106(1):380–93.
- [31] de Paly M et al. Optimization of energy extraction for closed shallow geothermal systems using linear programming. *Geothermics* 2012;43:57–65.
- [32] Taniguchi M et al. Disturbances of temperature-depth profiles due to surface climate change and subsurface water flow: 1. An effect of linear increase in surface temperature caused by global warming and urbanization in the Tokyo Metropolitan Area, Japan. *Water Resour Res* 1999;35(5):1507–17.
- [33] Ferguson G, Woodbury AD. Subsurface heat flow in an urban environment. *J Geophys Res: Solid Earth (1978–2012)* 2004;109(B2).
- [34] Epting J, Huggenberger P. Unraveling the heat island effect observed in urban groundwater bodies – definition of a potential natural state. *J Hydrol* 2013;501:193–204.
- [35] Zhu K et al. The geothermal potential of urban heat islands. *Environ Res Lett* 2010;5(4):044002.
- [36] Balke K. Das Grundwasser als Energieträger. *Brennstoff-Wärme-Kraft* 1977;29:191–4.
- [37] Huchtemann K, Müller D. Combined simulation of a deep ground source heat exchanger and an office building. *Build Environ* 2014;73:97–105.
- [38] Menberg K et al. Long-term evolution of anthropogenic heat fluxes into a subsurface urban heat island. *Environ Sci Technol* 2013;47(17):9747–55.
- [39] Müller N, Kuttler W, Barlag A-B. Analysis of the subsurface urban heat island in Oberhausen, Germany. *Climate Res* 2014;58(3):247–56.
- [40] Taylor CA, Stefan HG. Shallow groundwater temperature response to climate change and urbanization. *J Hydrol* 2009;375(3):601–12.
- [41] Santander J et al. Calculation of some integrals arising in heat transfer in Geothermics. *Math Problem Eng* 2010;2010.
- [42] Bandos TV et al. Finite line-source model for borehole heat exchangers: effect of vertical temperature variations. *Geothermics* 2009;38(2):263–70.
- [43] Duan X, Naterer GF. Ground heat transfer from a varying line source with seasonal temperature fluctuations. *J Heat Transfer* 2008;130(11):111302–111302.
- [44] Bonte M et al. Underground thermal energy storage: environmental risks and policy developments in the Netherlands and European Union. *Ecol Soc* 2011;16(1):22.
- [45] Bayer P et al. Greenhouse gas emission savings of ground source heat pump systems in Europe: a review. *Renew Sustain Energy Rev* 2012;16(2):1256–67.
- [46] Holmberg H et al. Numerical model for non-grouted borehole heat exchangers. Part 2-Evaluation. *Geothermics* 2014.
- [47] Diao N, Li Q, Fang Z. An analytical solution of the temperature response in geothermal heat exchangers with groundwater advection. *J Shandong Inst Arch Eng* 2003;3:000.
- [48] Zhang W et al. The heat transfer analysis and optimal design on borehole ground heat exchangers. *Energy Procedia* 2014;61:385–8.
- [49] Molina-Giraldo N, Bayer P, Blum P. Evaluating the influence of thermal dispersion on temperature plumes from geothermal systems using analytical solutions. *Int J Therm Sci* 2011;50(7):1223–31.
- [50] Hecht-Méndez J et al. Evaluating MT3DMS for heat transport simulation of closed geothermal systems. *Groundwater* 2010;48(5):741–56.
- [51] Özışık MN. *Boundary value problems of heat conduction*. Courier Corporation; 1989.
- [52] Schärli U, Rybach L. Determination of specific heat capacity on rock fragments. *Geothermics* 2001;30(1):93–110.
- [53] Philippe M, Bernier M, Marchio D. Validity ranges of three analytical solutions to heat transfer in the vicinity of single boreholes. *Geothermics* 2009;38(4):407–13.
- [54] Zhang Y, Soga K, Choudhary R. Shallow geothermal energy application with GSHPs at city scale: study on the City of Westminster. *Géotechnique Lett* 2014;4(April–June):125–31.
- [55] Angelotti A et al. Energy performance and thermal impact of a Borehole Heat Exchanger in a sandy aquifer: Influence of the groundwater velocity. *Energy Convers Manage* 2014;77:700–8.
- [56] Eugster W. *Erdwärmesonden-Funktionsweise und Wechselwirkung mit dem geologischen Untergrund*. 1991, Diss. Naturwiss. ETH Zürich, Nr. 9524; 1991.
- [57] Anderson MP. Heat as a ground water tracer. *Groundwater* 2005;43(6):951–68.
- [58] SFOMC. Swiss Federal Office of Meteorology and Climatology [cited 2014 September]; <[www.meteoswiss.admin.ch](http://www.meteoswiss.admin.ch)>.
- [59] Signorelli S, Kohl T. Regional ground surface temperature mapping from meteorological data. *Global Planetary Change* 2004;40(3):267–84.
- [60] Menberg K et al. Observed groundwater temperature response to recent climate change. *Hydrol Earth Syst Sci Discuss* 2014;11(3):3637–73.
- [61] Kurylyk BL, MacQuarrie KT. A new analytical solution for assessing climate change impacts on subsurface temperature. *Hydrol Process* 2013.
- [62] Tye-Gingras M, Gosselin L. Adapting design procedure for vertical ground heat exchangers to consider groundwater flow. *Renewable Energy* 2014: p. in preparation.